Materials Advances

PAPER

View Article Online
View Journal | View Issue

Cite this: *Mater. Adv.*, 2025, **6**, 7942

Exploring the adsorptive properties of an embryonic zeolite toward methylene blue

Rusi Rusew, *[ab] Hristina Lazarova, [ab] Magdalena Angelova,[ab]
Nevena Petkova-Yankova, [a] Rositca Nikolova[a] and Valentin Valtchev *[ac]

Textile dyes are persistent water pollutants, requiring effective treatment strategies. This study reports the adsorption performance of embryonic zeolite precursors (EZPs) synthesized with tetrapropylammonium hydroxide as a structure-directing agent. The materials were prepared with different Si/Al ratios (50, 100, and 200) in the starting gel and tested for the removal of methylene blue (MB) from aqueous solutions. Comprehensive characterization (PXRD, SAXS, BET, FTIR, EDXRF, N_2 physisorption, and TGA/DSC) confirmed their micro/mesoporous and amorphous nature. Among them, EZTPA50 displayed the highest surface area (915 m^2 g^{-1}) and hierarchical porosity. Adsorption experiments revealed that EZTPA50 and EZTPA100 outperformed the crystalline counterpart H-ZSM-5. Their monolayer capacities reached 146.08 mg g^{-1} and 122.62 mg g^{-1}, respectively. Langmuir isotherm modeling indicated monolayer coverage, while Elovich kinetics suggested heterogeneous surface chemisorption. Thermodynamic analysis showed spontaneous, endothermic, and entropy-driven adsorption for both materials. Intraparticle diffusion analysis revealed a multi-stage adsorption mechanism influenced by pore accessibility and surface heterogeneity. Thermal regeneration studies demonstrated that $EZ_{TPA}50$ retained ~90% removal efficiency over four cycles, highlighting its structural stability and reusability. These findings position EZPs – particularly $EZ_{TPA}50$ – as promising, regenerable adsorbents for efficient dye removal, offering advantages over conventional microporous zeolites in terms of adsorption capacity, kinetics, and thermal robustness.

Received 22nd August 2025,
Accepted 18th September 2025

DOI: 10.1039/d5ma00944h

rsc.li/materials-advances

Introduction

The textile industry is one of the largest contributors to water pollution, generating vast amounts of dye-laden wastewater during dyeing and finishing processes.[1,2] These synthetic dyes are often non-biodegradable and can persist in the environment, posing serious risks to aquatic life and human health.[3,4] Even at low concentrations, dyes can hinder sunlight penetration and oxygen transfer in water bodies, disrupting aquatic ecosystems. Conventional water treatment methods – such as coagulation–flocculation,[5] biological degradation,[6] activated sludge processes,[7] and even photodegradation[8] – are often inadequate for removing synthetic dyes due to their complex molecular structures and resistance to bio-photodegradation. These methods suffer from additional limitations such as excessive chemical use and sludge generation,[9] low effectiveness against non-biodegradable compounds,[10] sensitivity to toxic dye components along with demanding operational requirements,[11] and the need for specific light sources and longer exposure times.[12] Those limitations highlight the need for advanced remediation strategies to address textile dye pollution. Among the emerging alternatives, adsorptive materials such as zeolites have attracted significant attention due to their high efficiency, selectivity, and regeneration potential.[13]

Zeolites are crystalline aluminosilicate materials with highly ordered microporous frameworks, large internal surface areas, and exceptional adsorption and ion-exchange capabilities.[14,15] Their unique three-dimensional structure, composed of SiO_4 and AlO_4 tetrahedra connected by shared oxygen atoms, creates negatively charged frameworks upon substitution of Si^{4+} with Al^{3+}. These charges are typically balanced by exchangeable cations such as Na^+ or K^+, contributing to the high cation-exchange capacity and strong sorptive interactions with various charged species, including dyes and pharmaceuticals.[16,17] Owing to their thermal stability, chemical robustness, and tunable physicochemical properties, zeolites have been extensively studied for industrial and environmental applications.[18–21] However, the conventional zeolites are ultra-microporous materials with a pore size below 7.5 Å, which limits their applications to relatively small molecules. Additionally, their adsorption performance can be hindered by

---

[a] *University of Sofia, Faculty of Chemistry and Pharmacy, 1126 Sofia, Bulgaria*
[b] *Institute of Mineralogy and Crystallography Acad. I. Kostov, Bulgarian Academy of Sciences, Acad. G. Bonchev Str., bl. 107, 1113 Sofia, Bulgaria*
[c] *Normandie Univ, ENSICAEN, UNICAEN, CNRS, Laboratoire Catalyse et Spectrochimie, 6 Marechal Juin, 14050 Caen, France*

slow diffusion kinetics, limited accessibility of active sites for bulky dye molecules, and potential competitive adsorption from coexisting ions or natural organic matter in real wastewater matrices.[22]

In parallel, other advanced adsorbents such as engineered biochars,[23,24] metal–organic frameworks (MOFs),[25,26] and covalent organic frameworks (COFs)[27,28] have been actively investigated for dye and pharmaceutical removal. Biochars are low-cost and sustainable but often exhibit limited surface areas and heterogeneous adsorption sites. MOFs and COFs provide exceptionally high surface areas and tunable functionalities, yet their practical use is constrained by multi-step syntheses, high production costs, and in some cases insufficient hydrothermal stability. These considerations underscore the need for alternative adsorbents that combine high efficiency and tunability with simpler synthesis and greater scalability.

Embryonic zeolite precursors (EZPs) have recently emerged as promising materials that may overcome the drawbacks of conventional zeolites while addressing some of the limitations of other advanced adsorbents.[29–31] These intermediates, formed during the early stages of zeolite synthesis, exhibit partially ordered structures that combine features of amorphous gels and crystalline frameworks. This transitional morphology imparts several beneficial characteristics, including enhanced surface reactivity, high external surface area, and the presence of both mesopores and micropores – traits which improve the diffusion and adsorption of relatively large molecules.[31] Unlike fully crystallized zeolites, EZPs can be synthesized under milder conditions and shorter durations, offering energy-efficient and potentially scalable routes for functional adsorbent production.[29,32] Furthermore, their surface properties – including surface charge, silanol/aluminol content, and porosity – can be finely tuned by adjusting synthesis parameters or applying post-treatment modifications that could play a crucial role in governing host–guest interactions.

Despite these advantages, the use of EZPs in dye adsorption remains underexplored, especially relative to conventional zeolites, clays, or activated carbons.[33–38] A thorough review of the literature reveals a notable gap, with no prior studies systematically investigating EZPs for dye removal applications. Therefore, the present work represents a novel contribution by demonstrating, for the first time, the efficacy of EZP materials in adsorbing methylene blue (MB), highlighting their promising performance, reusability, and structural advantages over traditional microporous adsorbents. Moreover, a detailed understanding of the structure – function relationships that control MB uptake – such as surface charge distribution, pore accessibility, and adsorption energetics – is essential for guiding material optimization. This study aims to fill this gap by investigating the adsorption behavior of embryonic zeolite precursors toward methylene blue under aqueous conditions. Comprehensive characterization of the EZPs – covering surface area, pore structure, point of zero charge (PZC), and functional groups – will be combined with kinetic and equilibrium adsorption experiments to elucidate the mechanisms underlying MB removal. These insights will support the rational design of next-generation zeolite-based adsorbents with high efficiency, reusability, and applicability in dye-contaminated wastewater treatment.

Results and discussion

Synthetic procedures

Embryonic zeolite precursors were synthesized according to the protocol proposed by Akouche *et al.*[29] The molar ratio of the initial clear solution was 9TPAOH/xAl$_2$O$_3$/25SiO$_2$/430H$_2$O/100EtOH (x = 0.25, 0.50 and 1.0) where TPAOH is tetrapropylammonium hydroxide (40% aqueous solution) aluminum sulfate octadecahydrate (Al$_2$SO$_4$·18H$_2$O) used as Al-source, and tetraethyl orthosilicate (TEOS, 98%) as Si-source. The total amount of TPA-OH, aluminum sulphate, and ddH$_2$O was weighed in a polypropylene bottle. After complete dissolution of the aluminum sulphate, TEOS – was added to the mixture dropwise with constant stirring at room temperature. This ensures uniform hydrolysis and subsequent polymerization. After adding the entire amount of TEOS, the reaction solution was stirred at room temperature for 6 hours until a monophasic solution is obtained. After the completion of the hydrolysis step, the resulting solution was freeze-dried at 89 °C under vacuum ($<$0.055 mbar) to terminate the crystallization process. The white powdery substances obtained after freeze-drying were grounded and calcined in ceramic mortars at 550 °C for 8 hours to remove the organic template. Alternatively, ZSM-5 obtained from the same initial suspension (xAl$_2$O$_3$ = 0.25) at 100 °C for 48 h was used as reference. The white precipitate of ZSM-5 was obtained and washed with centrifugation (ddH$_2$O, 10 000 rpm, 3 × 20 min) and calcined at 550 °C for 8 h. Three embryonic zeolite precursors were obtained, differing by the Si/Al ratio of the initial clear solution. For clarity, the materials are denoted as: EZ$_{\text{TPA}}$200 (*i.e.*, Si/Al = 200), EZ$_{\text{TPA}}$100, and EZ$_{\text{TPA}}$50, respectively. The general procedure for the preparation of the embryonic zeolite precursors is given in Scheme 1.

Characterization of the materials

Powder X-ray diffraction (PXRD) and energy-dispersive X-ray fluorescence (EDXRF) analyses were used to evaluate the synthesis outcome of the EZPs. As expected, the PXRD patterns of the EZPs (Fig. S1) exhibit broad, low-intensity reflections indicative of their amorphous or short-range ordered nature. Although phase identification was not feasible due to the lack of sharp diffraction features, PXRD still served as a valuable tool to confirm the absence of undesired crystalline impurities. For comparison, the PXRD pattern of fully crystalline ZSM-5 (Fig. S1) is characterized by intense and well-defined reflections typical of the MFI topology.

The results from the EDXRF analysis of the embryonic samples (Table 1) revealed a systematic increase in Si content

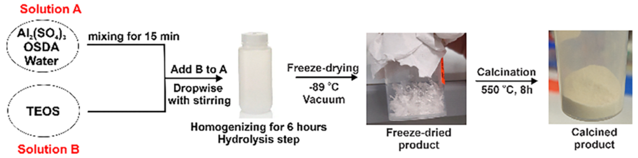

Scheme 1 General procedure for preparation of embryonic zeolite precursors of ZSM-5.

Table 1 Elemental composition of EZPs determined with energy-dispersive X-ray fluorescence (EDXRF)

	Si/Al ratio	Weigh, %		Si/Al ratio (±10% error)
	Starting mixture	Si	Al	Calcined products
$EZ_{TPA}50$	50	93.97	6.03	15.0 (1.5)
$EZ_{TPA}100$	100	96.55	3.45	26.9 (2.7)
$EZ_{TPA}200$	200	98.58	1.42	66.7 (6.7)
H-ZSM-5	200	98.21	1.79	52.7 (5.3)

Table 2 Surface and textural properties of the series of synthesized materials

	Si/Al ratio	Isotherm type	S_{BET} m^2 g^{-1}	S_{micro} m^2 g^{-1}	V_{micro} cm^3 g^{-1}	V_{total} cm^3 g^{-1}
$EZ_{TPA}50$	50	IV, H4	915	301	0.13	0.68
$EZ_{TPA}100$	100	Ib	753	695	0.33	0.37
$EZ_{TPA}200$	200	Ib	559	542	0.22	0.24
H-ZSM-5	200	IV, H4	478	380	0.15	0.51

and decrease in Al content across the EZP series, in line with the starting gel compositions. Silicon weight percentage increased from 93.97% to 98.58%, while aluminium decreased from 6.03% to 1.42% as the nominal Si/Al ratio increased from 50 to 200. The calculated Si/Al ratios in the calcined products ranged from 15.0 to 66.7, demonstrating effective modulation of framework composition through precursor formulation. The deviation from nominal gel values is typical for amorphous or partially condensed aluminosilicates, where aluminum incorporation may be incomplete. The obtained Si and Al weight percents and Si/Al molar ratio of ∼53 for H-ZSM-5 are comparable with the literature.[39,40]

Physisorption analysis of the EZPs reveals the strong impact of the initial Si/Al ratio on the surface and textural properties of the final material. The N_2-isotherms (Fig. 1) demonstrate that TPA-templated EZPs exhibit significant changes in pore structure as the Si/Al ratio increases, directly impacting their potential for dye uptake. Surface properties of the studied materials are summarized in Table 2. At a Si/Al = 50, $EZ_{TPA}50$ displays a type IV isotherm with an H4-type hysteresis loop, indicating the presence of mesoporosity and slit-like pores. This is further supported by its broad DFT-derived pore size distribution (Fig. S2), which spans from micropores (∼1.3 nm) to a wide range of mesopores, including distinct populations at 2.0, 2.4, 3.1, 3.7, and even 5.1 nm. Such hierarchical porosity facilitates rapid diffusion and high-capacity adsorption of bulky organic dyes. Consistently, $EZ_{TPA}50$ shows the highest BET surface area (915 m^2 g^{-1}) and total pore volume (0.68 cm^3 g^{-1}), although only a portion of this surface is microporous (S_{micro} = 301 m^2 g^{-1}; V_{micro} = 0.13 cm^3 g^{-1}). With increasing Si/Al ratios (100 and 200), the isotherms transition to type I(b), typical of microporous frameworks.

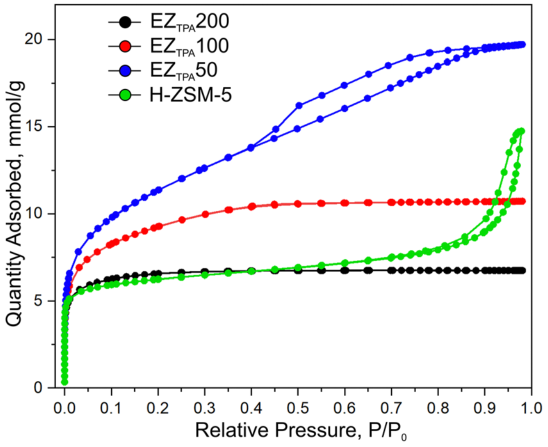

Fig. 1 N_2 adsorption isotherms of embryonic zeolite (EZ) samples synthesized with TPA-OH and Si/Al ratio of the starting mixture = 50, 100, 200, and H-ZSM-5.

$EZ_{TPA}100$ exhibits dominant peaks around 0.84, 1.23, and 1.93 nm, along with a reduced presence of mesopores, reflected in its smaller total pore volume (0.37 cm^3 g^{-1}). This suggests a more ordered but less accessible framework. $EZ_{TPA}200$ displays a similar trend, with narrow micropore populations centered around 0.82, 1.10, 1.55, 1.90, and 2.27 nm, consistent with highly condensed and uniform microporous domains. The reduction in total surface area (559 m^2 g^{-1}) and pore volume (0.24 cm^3 g^{-1}) further indicates decreased accessibility for larger adsorbates. Notably, the H-ZSM-5 sample exhibits an N_2 adsorption isotherm of type IV with an H4 hysteresis loop, consistent with the coexistence of micropores and additional mesoporosity or interparticle voids. While classical ZSM-5 is typically described by a type I isotherm due to its strictly microporous channel system, deviations toward type IV with hysteresis have frequently been reported for nanosized or aggregated ZSM-5 crystals.[41,42] The steep uptake at low relative pressures (P/P_0 < 0.1) confirms efficient micropore filling, whereas the hysteresis loop observed at intermediate relative pressures (P/P_0 ≈ 0.45–0.9) reflects secondary porosity associated with crystal aggregation. This interpretation is supported by the textural parameters in Table 2, where the micropore volume (0.15 cm^3 g^{-1}) accounts for only part of the total pore volume (0.51 cm^3 g^{-1}). The DFT pore size distribution (Fig. S2) confirms a narrow micropore population below 1 nm, typical for MFI-type frameworks. H-ZSM-5 demonstrates a lower total adsorbed quantity compared to the mesoporous-rich $EZ_{TPA}50$, reflecting its compact and highly ordered microporous framework. These findings underscore how tailored synthesis conditions enable control over textural properties, which are critical for optimizing adsorption behavior. Materials like $EZ_{TPA}50$, with a balance of micro- and mesoporosity, may be better suited for high-capacity and fast adsorption of dyes. In contrast, higher-silica or more crystalline materials offer more defined binding environments for selective uptake.

The FTIR spectra of the synthesized materials (Fig. S3) reveal clear distinctions between the EZPs ($EZ_{TPA}200$, $EZ_{TPA}100$, $EZ_{TPA}50$) and the fully crystalline H-ZSM-5. All samples display strong bands at ∼1230 cm^{-1} and 1080–1100 cm^{-1}, corresponding to external and internal asymmetric stretching vibrations of Si–O–Si and Si–O–Al type, as well as symmetric Si–O–Si stretching bands at 800–850 cm^{-1}, confirming the presence of a silicate-based framework. A shoulder near 960 cm^{-1}, more prominent in the EZPs, is attributed to Si–OH groups or framework defects, suggesting incomplete network condensation. Notably, the MFI-specific band at ~550 cm^{-1} – associated with vibrations of double five-membered rings – is clearly observed in H-ZSM-5 but almost absent in all EZPs, indicating a lack of long-range structural order. Additionally, broad O–H stretching near 3450 cm^{-1} and a bending mode at ~1630 cm^{-1} confirm the presence of physisorbed water. These observations support the classification of the EZPs as pre-crystalline intermediates with underdeveloped MFI topology but with accessible silanol-rich surfaces favorable for adsorption processes.

The ^{29}Si and ^{27}Al NMR spectra of EZ$_{TPA}$50, EZ$_{TPA}$100, EZ$_{TPA}$200 and H-ZSM-5 are shown on Fig. S4. ^{29}Si MAS NMR of EZ$_{TPA}$50, EZ$_{TPA}$100 and EZ$_{TPA}$200 shows broad Q^4 (−105 to −115 ppm) and Q^3 (−95 ppm) resonances, indicating a disordered, partially condensed silicate network, whereas H-ZSM-5 exhibits sharp, well-resolved Q^4 peaks typical of the MFI framework. The similar ^{29}Si profiles of the EZPs confirm their common amorphous/pre-crystalline nature. ^{27}Al MAS NMR of the EZPs features a broad tetrahedral AlO$_4$ signal (~60–70 ppm) and an intense octahedral AlO$_6$ peak (~0 ppm), consistent with incomplete Al incorporation and significant extra-framework species. H-ZSM-5 is dominated by framework AlO$_4$ with traces of AlO$_6$, reflecting efficient Al incorporation into the lattice. These results highlight the higher defect density and extra-framework Al content in EZPs compared to crystalline H-ZSM-5.

The EZPs are too small to be studied by scanning electron microscopy. We have employed transmission electron microscopy (TEM) to study their intimate structure. Different magnification electron micrographs of EZ$_{TPA}$50 sample are given on Fig. S5. Agglomerates with sizes ranging between one and several microns were observed. High magnification images revealed that the agglomerates are built up of much smaller particles with size of several nanometers. The presence of textural mesopores between the aluminosilica particles is clearly observable. No traces of a crystalline material were found.

The volume-weighted particle size distributions obtained from SAXS for the EZ$_{TPA}$ materials synthesized with Si/Al ratios of 50, 100, and 200 (H-ZSM-5 is not nanosized) are given on Fig. S6. EZ$_{TPA}$50 shows the broadest distribution and largest average radius (33 Å), characterized by a log-normal fit, which reflects significant size heterogeneity and less controlled nucleation. In contrast, EZ$_{TPA}$100 and EZ$_{TPA}$200 display narrower, symmetric Gaussian distributions with reduced average radii of 21 Å and 20 Å, respectively, indicating more uniform and refined particle populations. This trend correlates with increasing silica content in the synthesis mixture, which appears to promote homogeneous nucleation and suppress structural disorder introduced by aluminium. The surface-to-volume (S/V) ratio also increases with silica content, rising from 0.12 Å^{-1} for EZ$_{TPA}$50 to 0.20 Å^{-1} for EZ$_{TPA}$200 (Table 3), further highlighting the emergence of smaller, more surface-accessible particles. The observed nanoscale morphological differences are significant for adsorption performance. Finer, uniformly distributed particles with higher S/V ratios, such as those in EZ$_{TPA}$200, may provide better dispersion in aqueous environments and faster surface interactions, whereas larger, more polydisperse particles like those in EZ$_{TPA}$50 might offer higher loading capacities but slower kinetics. These SAXS results underscore the pivotal role of Si/Al ratio in tuning particle size, distribution, and functional performance of embryonic zeolites.

Table 3 Summary from the SAXS experiment on the series of embryonic zeolites

Sample	Si/Al ratio	Average radius Å	S/V ratio Å^{-1}	Size distribution model fit
EZ$_{TPA}$50	50	33	0.12	Log-normal
EZ$_{TPA}$100	100	21	0.17	Gaussian
EZ$_{TPA}$200	200	20	0.20	Gaussian

Thermal analysis of the calcined EZPs was performed using TGA/DSC to evaluate their residual surface chemistry and water adsorption behavior. Prior to the measurements, the samples were equilibrated at 90% relative humidity (RH) for 24 hours to ensure saturation of surface-adsorbed water and enable comparative assessment of water uptake capacity. As shown in Fig. S7 the TGA curves reveal two main weight loss regions. The initial weight loss below 150 °C, corresponding to 18–31 wt% depending on the sample, is attributed to desorption of physisorbed water. This is confirmed by a broad endothermic signal observed in the DSC, centered around 120–150 °C. The extent of water loss decreases with increasing Si/Al ratio, indicating that aluminum-rich samples (*e.g.*, EZ$_{TPA}$50) retain more surface-bound water, likely due to a higher density of hydrophilic sites (Si–OH and Al–OH groups). A secondary, gradual mass loss (3–4 wt%) occurs between 200 and 350 °C, more pronounced in EZ$_{TPA}$50. Since the samples were pre-calcined at 550 °C for 8 hours to remove organic templates, this second step is not due to organic decomposition. Instead, it likely corresponds to dehydroxylation of structural –OH groups and desorption of residual species such as carbonates or chemisorbed water.[43,44] No significant weight changes are observed above 400 °C, confirming the thermal stability of the framework. These results underscore the greater water uptake capacity of low-silica EZPs, which may influence their adsorption behavior. Moreover, the thermal stability of the EZPs up to 550–600 °C is advantageous for repeated regeneration cycles, ensuring structural integrity and sustained performance.

Adsorption studies

Adsorption experiments were conducted using methylene blue (MB) as a model cationic dye to evaluate the performance of the EZPs. Batch kinetic studies were performed to evaluate the influence of contact time, adsorbent dosage, initial dye concentration, initial pH, and temperature on the adsorption rate. In all experiments (unless otherwise stated), a fixed adsorbent dosage of 25 mg in 50 mL of MB aqueous solution containing 0.01 M NaCl was used. Performing the experiments in 0.01 M NaCl ensures minimal pH drift, control of ionic strength, reduction in variability, and enhancement of the reliability of adsorption data by simulating real conditions without interfering with the adsorption mechanism. The suspensions were stirred at 250 rpm in 200 mL beakers and maintained at 25 °C. Samples were centrifuged at 14 000 rpm for 1 min, and residual MB concentrations were determined spectrophotometrically by measuring the absorption of MB at $\lambda_{\max} = 664$ nm and derived from the calibration curve (Fig. S8). All experiments were performed in triplicate, and the average values were used for analysis. The equilibrium adsorption capacities (q_e, mg g^{-1}) and removal efficiencies (R, %) were calculated using eqn (1) and (2):

$$q_e = \frac{(C_0 - C_e)V}{m} \tag{1}$$

$$R = \frac{(C_0 - C_e)}{C_0} \times 100 \tag{2}$$

where C_0 and C_e are the initial and equilibrium concentrations of MB, respectively, V (L) is the solution volume, and m (g) is the mass of the adsorbent.

Effect of contact time on removal efficiency

Contact time studies were performed to determine the time required to reach adsorption equilibrium under standard conditions. The effect of contact time on the adsorption capacity and removal efficiency of EZPs and H-ZSM-5 is given in Fig. 2. Samples $EZ_{TPA}100$ and $EZ_{TPA}50$ achieved the highest removal efficiencies of 71.96% and 80.40% respectively, in comparison to $EZ_{TPA}200$ and H-ZSM-5 with 18.62% and 52.60%. The equilibrium was reached at 4 h in all cases with minimal MB adsorption afterwards. Due to the achieved better performance, $EZ_{TPA}100$ and $EZ_{TPA}50$ were used in the subsequent optimization studies focused on the effect of initial pH, adsorbent dosage, and initial MB concentration on adsorption. The equilibrium time was fixed at 4 h in all experiments.

Effect of initial pH on adsorption

The pH of the solution plays a critical role in adsorption processes by influencing both the surface charge of the adsorbent and the ionization state of the adsorbate. Understanding this relationship is essential for optimizing removal efficiency, particularly when electrostatic interactions govern the adsorption mechanism.

The point of zero charge (pH_{PZC}) is an important surface property that defines the pH at which the net surface charge of an adsorbent is neutral.[45] At pH < pH_{PZC}, the surface is predominantly positively charged, while at pH > pH_{PZC} it becomes negatively charged. This has significant implications for adsorption behavior, particularly for ionic contaminants such as dyes and pharmaceuticals. The pH_{PZC} values of $EZ_{TPA}100$ and $EZ_{TPA}50$ were determined using the pH drift method. Each suspension contained 10 mg of adsorbent dispersed in 10 mL 0.01 M NaCl solution, initially adjusted to pH values ranging from 2 to 10 using 0.1 M NaOH or 0.1 M HCl. After 24 h of stirring, the supernatants were centrifuged, the final pH was measured, and ΔpH ($pH_{initial}$–pH_{final}) was plotted as a function of the initial pH. The pH_{PZC} was identified as the point where ΔpH = 0 (Fig. 3).

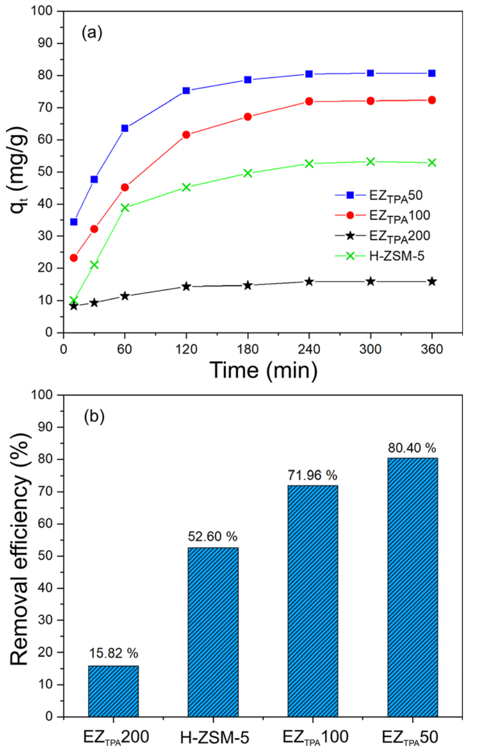

Fig. 2 Time-dependent adsorption of MB onto different adsorbents (a) and (b) removal efficiency for each material after 4 h of contact time. Experimental conditions: initial MB concentration = 50 mg L^{-1}, adsorbent dosage = 25 mg, V = 50 mL, pH (unadjusted) = 5.6, 0.01 M NaCl, stirring speed = 250 rpm and T = 25 °C.

The obtained values for pH_{PZC} are 3.80 and 3.11 for $EZ_{TPA}100$ and $EZ_{TPA}50$, respectively. These results show that both EZP samples exhibit low pH_{PZC} values, consistent with the presence of silanol (Si–OH) and aluminol (Al–OH) groups that tend to deprotonate at moderately acidic pH. Moreover, a slight trend is observed where decreasing the Si/Al ratio (*i.e.*, increasing aluminum content) lowers the pH_{PZC}, suggesting that a higher concentration of framework Al leads to increased surface acidity (*e.g.*, $EZ_{TPA}50$). These findings are important for understanding electrostatic interactions between the EZP surface and adsorbates. For example, at pH > pH_{PZC}, the negatively charged surface will favor the adsorption of cationic species such as methylene blue, while repelling anionic compounds. The effect of $pH_{initial}$ on MB adsorption by $EZ_{TPA}100$ and $EZ_{TPA}50$ was investigated by adjusting the pH from 2 to 8, while keeping all other parameters constant (Fig. 4). Indeed, the removal efficiency for both $EZ_{TPA}100$ and $EZ_{TPA}50$ increases with pH, confirming that electrostatic interactions between the positively charged molecule of methylene blue and the negatively charged EZP surface play a crucial role in adsorption efficiency. The maximum adsorption of methylene blue for both $EZ_{TPA}100$ and $EZ_{TPA}50$ occurred at pH = 7, likely due to optimal electrostatic interactions between the cationic dye and

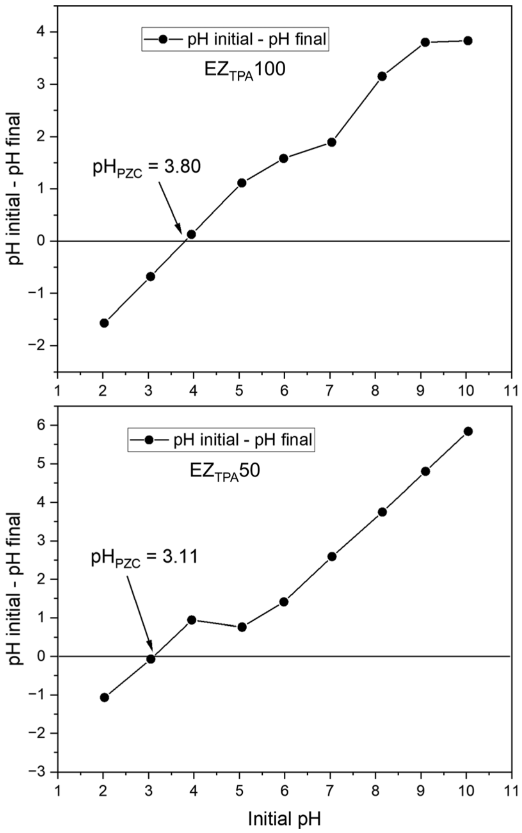

Fig. 3 pH$_{PZC}$ graphs of EZ$_{TPA}$50 and EZ$_{TPA}$100.

the negatively charged adsorbent surface. The slight decrease in adsorption efficiency at higher pH values may result from increased OH$^-$ competition, ionic shielding, or dye aggregation effects that reduce the availability of active adsorption sites.[46,47]

Effect of adsorbent dosage on adsorption

The influence of adsorbent dosage was evaluated by varying the mass of the material from 5 to 50 mg, while keeping the dye concentration, volume, temperature, and pH constant (Fig. 5). For both EZ$_{TPA}$50 and EZ$_{TPA}$100, the adsorption efficiency of methylene blue increased with increasing adsorbent dosage. At lower dosages (5–20 mg), EZ$_{TPA}$50 consistently showed higher removal efficiency than EZ$_{TPA}$100, suggesting a more accessible or active surface. As the dosage increased, both materials approached saturation, reaching over 90% removal at 50 mg. Although almost a complete dye removal was achieved at 50 mg concentration, a working dosage of 25 mg was selected for the subsequent kinetic, adsorption isotherm, and thermodynamic studies. This intermediate dosage enables measurable variations in equilibrium concentration and adsorption capacity, which are essential for accurately evaluating adsorption behavior over time, modeling equilibrium interactions, and calculating thermodynamic parameters such as ΔG°, ΔH°, and ΔS°. Moreover, a 25 mg dosage provides a good balance between high removal efficiency and analytical sensitivity across the studied conditions.

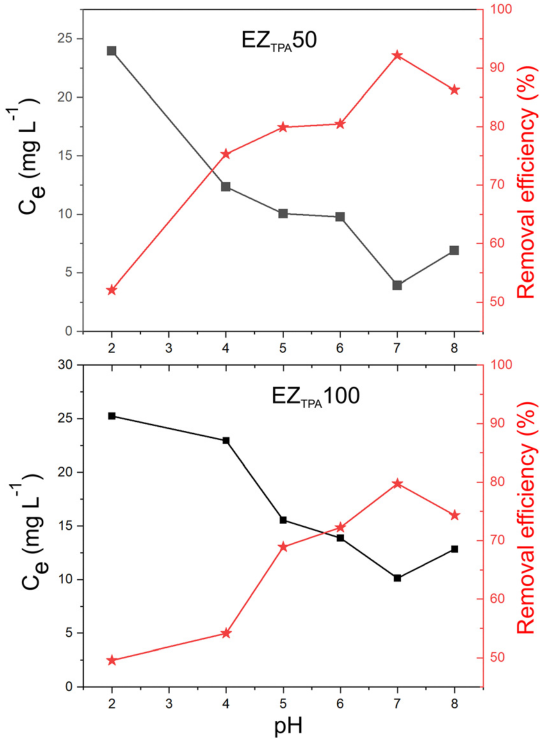

Fig. 4 Effect of different values of initial pH on the adsorption of MB onto EZTPA50. Experimental conditions: initial MB concentration = 50 mg L^{-1}, adsorbent dosage = 25 mg, V = 50 mL, 0.01 M NaCl, stirring speed = 250 rpm, T = 25 °C and time = 4 h.

Adsorption isotherms

Adsorption isotherm experiments were conducted to evaluate the equilibrium interaction between methylene blue (MB) and the adsorbents (EZ$_{TPA}$50, EZ$_{TPA}$100, EZ$_{TPA}$200, and H-ZSM-5). These studies are important for understanding the adsorption capacity and the nature of the adsorbate–adsorbent interaction

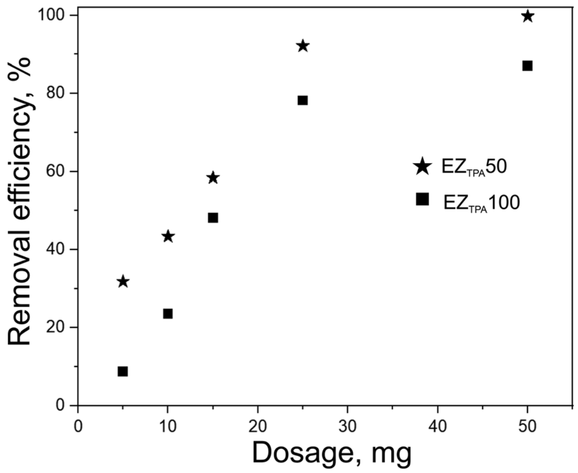

Fig. 5 The effect of EZ$_{TPA}$100 and EZ$_{TPA}$50 dosage on MB removal efficiency. Experimental conditions: initial MB concentration = 50 mg L^{-1}, V = 50 mL, pH = 7, 0.01 M NaCl, stirring speed = 250 rpm, T = 25 °C and time = 4 h.

at a constant temperature. Batch adsorption experiments were conducted at 25 °C and pH = 7 by varying the initial concentration of methylene blue in the range of 20–200 mg L^{-1} while maintaining a constant adsorbent dose (25 mg, 0.5 g L^{-1}).

Although kinetic studies showed that equilibrium was reached within 4 hours at lower MB concentrations (up to 60 mg L^{-1}), preliminary isotherm trials with both $EZ_{TPA}50$ and $EZ_{TPA}100$ at higher MB concentrations (>80 mg L^{-1}) showed incomplete adsorption within 4 hours (Fig. 6). Therefore, a conservative equilibrium contact time of 24 h was adopted for all isotherm experiments to ensure complete saturation and accurate capacity measurements across the full concentration range.

The equilibrium adsorption data of methylene blue (MB) onto the studied materials were evaluated using the non-linear Langmuir, Freundlich, and Temkin isotherm models (Fig. 7). Each model provides insight into the nature of the adsorption process and the properties of the adsorbent surface. The fitting parameters and corresponding correlation coefficients (R^2) are summarized in Table 4. Non-linear adsorption isotherm fitting is preferred because it preserves the original mathematical form of the isotherm models without requiring linearization,

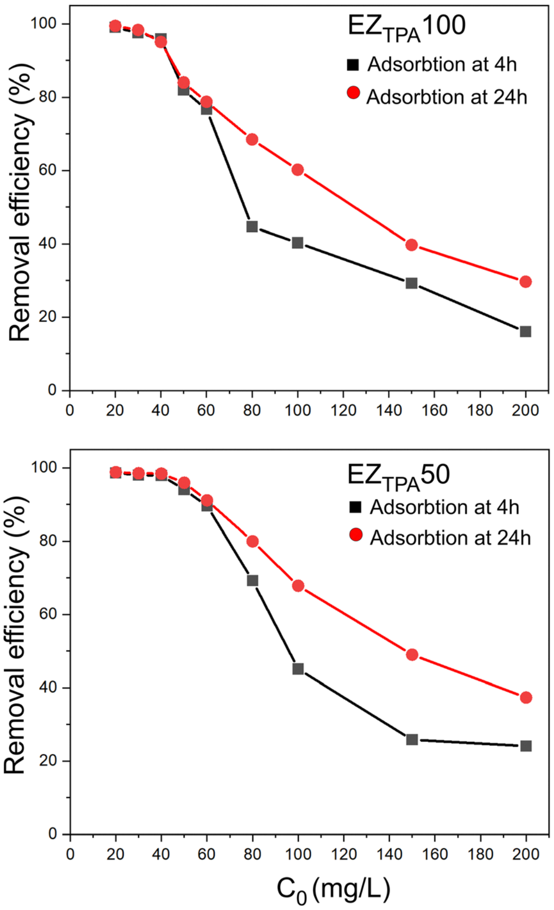

Fig. 6 Removal efficiency of methylene blue as a function of initial concentration (C_0) after adsorption on $EZ_{TPA}100$ (left) and $EZ_{TPA}50$ (right) at contact times of 4 h (black squares) and 24 h (red circles). Experimental conditions: adsorbent dosage 25 mg, solution volume 50 mL, background electrolyte = 0.01 M NaCl, pH = 7, T = 25 °C, stirring speed 250 rpm.

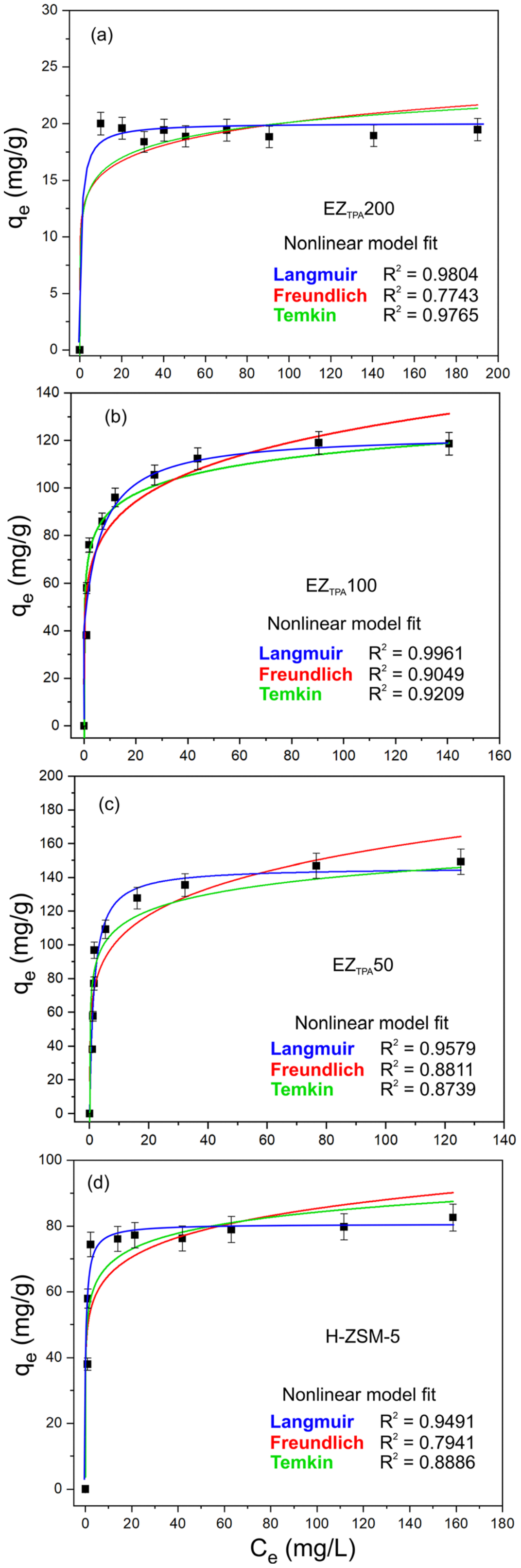

Fig. 7 Langmuir, Freundlich, and Temkin non-linear isotherm model fit for $EZ_{TPA}200$ (a), $EZ_{TPA}100$ (b), $EZ_{TPA}50$ (c) and H-ZSM-5 (d). Experimental conditions: adsorbent dosage 25 mg, solution volume 50 mL, background electrolyte = 0.01 M NaCl, pH = 7, T = 25 °C, stirring speed 250 rpm, time = 24 h.

Table 4 Adsorption isotherm fit parameters and estimated surface coverage (SMB) for methylene blue onto $EZ_{TPA}200$, $EZ_{TPA}100$, $EZ_{TPA}50$ and H-ZSM-5

Parameter		$EZ_{TPA}200$	$EZ_{TPA}100$	$EZ_{TPA}50$	H-ZSM-5
Langmuir isotherm model					
q_m	mg g^{-1}	19.75	122.62	146.08	80.53
K_L	L mg^{-1}	[a]	0.16	0.68	1.72
R^2		0.9804	0.9961	0.9579	0.9491
Freundlich isotherm model					
K_F	mg g^{-1} (L $mg)^{-1/n}$	11.80	56.76	68.38	49.41
n		8.64	5.90	5.51	8.42
R^2		0.7743	0.9049	0.8811	0.7941
Temkin isotherm model					
A	L mg^{-1}	315.07	382.04	274.21	1666.33
B	mg g^{-1}	1.94	10.92	13.16	7.01
R^2		0.9765	0.9209	0.8739	0.8886
Surface coverage (S_{MB})/BET surface		8.65%	60.5%	59.3%	62.6%

[a] Unreliable due to flatness of the isotherm.

which can distort error structure and introduce bias.[48,49] It provides more accurate parameter estimation, especially when data span a wide concentration range or exhibit strong curvature. Additionally, non-linear fitting avoids transformation-related artefacts and allows for better statistical evaluation of model performance.[48,49]

The Langmuir isotherm assumes monolayer adsorption on a homogenous surface with a finite number of identical adsorption sites. It is expressed in its non-linear form as:

$$q_e = \frac{q_{\max} K_L C_e}{1 + K_L C_e} \tag{3}$$

where $q_{\max}$ (mg g^{-1}) is the maximum adsorption capacity and K_L (L mg^{-1}) is the Langmuir constant related to the affinity of binding sites.

The Freundlich isotherm is an empirical model describing adsorption on heterogeneous surfaces. Its non-linear form is given by:

$$q_e = K_F C_e^{1/n} \tag{4}$$

where K_F [(mg g^{-1} (mg $l)^{-1/n}$] and n are the Freundlich constants indicating adsorption capacity and intensity, respectively.

The Temkin isotherm considers adsorbent–adsorbate interactions and assumes that the heat of adsorption decreases linearly with coverage. The non-linear form of the Temkin equation is:

$$q_e = B\ln(AC_e) \tag{5}$$

where A (L g^{-1}) is the Temkin isotherm constant, $B = RT/b$ (J mol^{-1}) is related to the heat of adsorption, R is the gas constant (8.314 J mol^{-1} K^{-1}), and T is the temperature (K).

The Langmuir model provided excellent correlation coefficients (R^2) for all four materials: $EZ_{TPA}200$ (R^2 = 0.9804), $EZ_{TPA}100$ (R^2 = 0.996), $EZ_{TPA}50$ (R^2 = 0.958), and H-ZSM-5 (R^2 = 0.949), indicating that surface saturation processes primarily govern MB adsorption. Among the tested materials, $EZ_{TPA}50$ exhibited the highest monolayer adsorption capacity (q_m = 146.08 mg g^{-1}), followed by $EZ_{TPA}100$ (q_m = 122.49 mg g^{-1}), H-ZSM-5 (q_m = 80.53 mg g^{-1}), and $EZ_{TPA}200$ (q_m = 19.75 mg g^{-1}). The Langmuir affinity constants K_L decrease in the following order: H-ZSM-5 (1.72 L mg^{-1}) > $EZ_{TPA}50$ (0.68 L mg^{-1}) > $EZ_{TPA}100$ (0.16 L mg^{-1}). The K_L calculation for $EZ_{TPA}200$ provided unreliable results due to the flatness of the adsorption isotherm (K_L ∼ 16.53 L mg^{-1}). Although H-ZSM-5 exhibits a significantly higher Langmuir constant, indicating a stronger affinity for methylene blue, its maximum adsorption capacity is considerably lower than that of $EZ_{TPA}50$ and $EZ_{TPA}100$. This indicates that while the surface of H-ZSM-5 has highly active or selective adsorption sites, their total number is limited, possibly due to its more ordered crystalline structure and lower external surface area or porosity. In contrast, the amorphous nature of $EZ_{TPA}50$ and $EZ_{TPA}100$ may provide a greater number of accessible adsorption sites, which despite slightly weaker individual dye–sorbent interactions results in much higher overall dye uptake.

The Freundlich isotherm model, which accounts for heterogeneous surface adsorption and multilayer interactions, provided acceptable fits for all materials, though with slightly lower R^2 values compared to the Langmuir model. Among the samples, $EZ_{TPA}100$ displayed the best Freundlich fit with R^2 = 0.9049, followed by $EZ_{TPA}50$ (R^2 = 0.8811) and H-ZSM-5 (R^2 = 0.7941). The Freundlich constant K_F was highest for $EZ_{TPA}50$ (68.38 mg g^{-1} (L $mg)^{-1/n}$), indicating a greater adsorption capacity on heterogeneous sites. Interestingly, H-ZSM-5 exhibited the highest Freundlich exponent n = 8.42, suggesting very favorable adsorption despite its lower K_F, which aligns with its strong affinity constant in the Langmuir model.

The Temkin model, which considers the effect of adsorbent–adsorbate interactions and a linear decrease in adsorption heat with coverage, also provided reasonable fits with R^2 values above 0.87 for all materials. The binding energy constant A was highest for H-ZSM-5 (1666.33 L mg^{-1}), significantly exceeding that of $EZ_{TPA}50$ and $EZ_{TPA}100$, reflecting the strong initial interaction between MB and H-ZSM-5's surface. However, the Temkin B constant, related to adsorption capacity, was lower for H-ZSM-5 (7.01 mg g^{-1}) compared to $EZ_{TPA}50$ (13.16 mg g^{-1}) and $EZ_{TPA}100$ (10.92 mg g^{-1}), consistent with its lower q_m in the Langmuir model. This further supports the interpretation that while H-ZSM-5 offers stronger binding affinity, its overall capacity is limited by fewer available sites. Overall, the isotherm analysis reveals that both embryonic zeolite precursors ($EZ_{TPA}50$ and $EZ_{TPA}100$) exhibit significantly improved adsorption performance compared to conventional ZSM-5. $EZ_{TPA}50$ in particular demonstrated the best overall performance, combining high adsorption capacity, favorable interaction strength, and surface heterogeneity.

The extent to which methylene blue (MB) molecules cover the surface of the adsorbent can be quantitatively estimated based on the monolayer adsorption capacity q_m obtained from Langmuir isotherm fitting. This approach allows direct comparison between the dye-covered surface and the BET-specific surface area, offering insight into adsorption efficiency and accessibility of active sites. By considering the molecular dimensions of MB and using Avogadro's number, the specific surface area occupied by adsorbed MB molecules (S_{MB}) can be calculated using the following expression:

$$S_{\mathrm{MB}} = \frac{q_{\mathrm{m}} A_{\mathrm{MB}} N_{\mathrm{Av}}}{M} \quad (6)$$

where A_{MB} is the surface area occupied by a single MB molecule (197.2 Å^2), N_{Av} is the Avogadro's number (6.022×1023 mol^{-1}) and M is the molar mass of MB (319.8 g mol^{-1}).

The calculated MB-covered surface areas (S_{MB}) were 542.8, 455.3, 299.1 m^2 g^{-1} and 48.34 m^2 g^{-1} for EZ$_{\mathrm{TPA}}$50, EZ$_{\mathrm{TPA}}$100, H-ZSM-5 and EZ$_{\mathrm{TPA}}$200, respectively. These values represent the maximum surface area that could be occupied by a monolayer of dye molecules, assuming flat molecular orientation and uniform distribution. When normalized against the respective BET surface areas, the fractional surface coverage was found to be 59.3% for EZ$_{\mathrm{TPA}}$50, 60.5% for EZ$_{\mathrm{TPA}}$100, 62.6% for H-ZSM-5, and only 8.65% for EZ$_{\mathrm{TPA}}$200. Despite its lower absolute adsorption capacity, H-ZSM-5 exhibited the highest relative surface utilization, consistent with its microporous nature and well-defined channel structure that promotes efficient packing of small adsorbates. In contrast, the mesoporous-rich EZ$_{\mathrm{TPA}}$50 showed the highest S_{MB} but a slightly lower fractional coverage, likely due to the contribution of mesopores and external surface area that are not fully accessible or effectively occupied by MB molecules. The results confirm that embryonic zeolite precursors possess higher overall accessibility and adsorption capacity for methylene blue compared to crystalline H-ZSM-5, supporting their potential as effective adsorbents. While their slightly lower fractional surface coverage reflects less efficient molecular packing—likely due to structural disorder and heterogeneous pore environments—this does not diminish their practical performance. Instead, it highlights the importance of further optimizing framework structure and composition to maximize both capacity and surface utilization efficiency. The markedly lower adsorption capacity and surface coverage observed for EZ$_{\mathrm{TPA}}$200 can be attributed to its dominant micropore population below ~1.0 nm, which restricts access of methylene blue molecules due to steric limitations. As a result, much of its surface area remains inaccessible to MB, leading to inefficient utilization despite a high BET surface area.

Adsorption kinetics

The adsorption kinetics of methylene blue (MB) onto the EZ$_{\mathrm{TPA}}$100 and EZ$_{\mathrm{TPA}}$50 were investigated to assess the rate and mechanism of dye uptake at different time intervals. In each experiment, 25 mg of the adsorbents were dispersed in 50 mL of MB solution with an initial dye concentration of 50 μg mL^{-1} and an initial pH = 7. The suspensions were stirred at 25 °C (250 rpm), and aliquots were taken at selected time intervals for UV-vis analysis. The kinetic data was analyzed using four widely accepted kinetic models: non-linear pseudo-first-order (PFO), pseudo-second-order (PSO), Elovich presented on Fig. 8, and intraparticle diffusion (IPD, Weber–Morris) model presented on Fig. 9. The corresponding fitting parameters are summarized in Table 5.

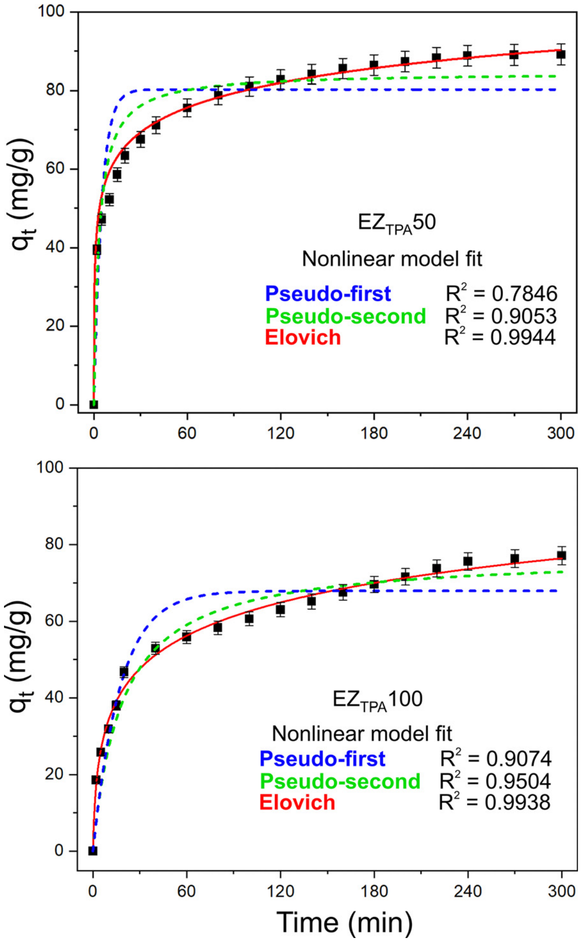

Fig. 8 Non-linear pseudo-first, pseudo-second, and Elovich model fit for EZ$_{\mathrm{TPA}}$50 and EZ$_{\mathrm{TPA}}$100. Experimental conditions: adsorbent dosage 25 mg, solution volume 50 mL, background electrolyte = 0.01 M NaCl, pH = 7, T = 25 °C, stirring speed 250 rpm.

The PFO model assumes that the rate of occupation of adsorption sites is proportional to the number of unoccupied sites.[50] It is typically valid for early stages of adsorption. The nonlinear form of the equation is:

$$q_t = q_{\mathrm{e}}(1 - \mathrm{e}^{-k_1 t}) \quad (7)$$

where q_{e} and q_t (mg g^{-1}) are the adsorption capacities at equilibrium and at time t (min), respectively, and k_1 (min^{-1}) is the rate constant of the PFO model.

The PSO model assumes that the adsorption follows second-order chemisorption.[50] It is given in its non-linear form as:

$$q_t = \frac{q_{\mathrm{e}}{}^2 k_2 t}{1 + q_{\mathrm{e}} k_2 t} \quad (8)$$

where k_2 (g mg^{-1} min^{-1}) is the rate constant of the PSO model.

The Elovich model is used for systems where the adsorption surface is heterogeneous. It describes chemisorption on highly active heterogeneous surfaces with non-uniform energy

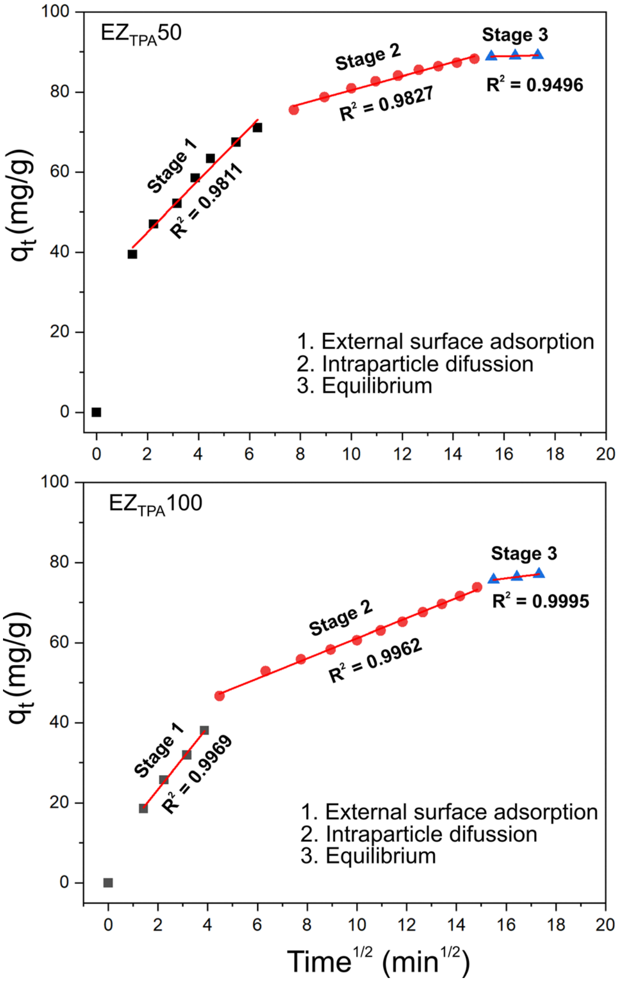

Fig. 9 Intraparticle diffusion model fit (Weber–Morris model) for EZ$_{TPA}$100 and EZ$_{TPA}$50.

distribution.[51] It is given in its nonlinear form as:

$$q_t = \frac{1}{\beta}\ln(1 + \alpha\beta t) \tag{9}$$

where α is the initial adsorption rate (mg g^{-1} min^{-1}), β is desorption constant related to surface coverage and activation energy (mg g^{-1}).

The IPD model considers the possibility that the adsorption process is controlled by the diffusion of MB molecules into the pores of the adsorbent.[52] The equation is expressed as:

$$q_t = k_{id}t^{1/2} + C \tag{10}$$

where, k_{id} (mg g^{-1} min$^{-1/2}$) is the intraparticle diffusion rate constant, and C (mg g^{-1}) is a constant that provides information about the boundary layer thickness. If the plot of q_t *versus* $t^{1/2}$ is linear and passes through the origin, intraparticle diffusion is the sole rate-limiting step. Otherwise, multiple processes may control adsorption.

For EZ$_{TPA}$50, the PFO model yielded a relatively poor fit with an R^2 = 0.7846 and a significant mismatch between the calculated and experimental equilibrium adsorption capacities (q_e = 80.27 mg g^{-1} *vs.* $q_{e,exp}$ = 89.23 mg g^{-1}). This suggests that simple physisorption governed by diffusion alone is not the dominant mechanism. The PSO model improved the fit substantially (R^2 = 0.9053), with a closer match between the theoretical and experimental q_e values (84.54 *vs.* 89.23 mg g^{-1}), implying that chemisorption involving electron sharing or exchange may contribute to the rate-controlling mechanism. However, the best fit was obtained using the Elovich model, which gave the highest correlation coefficient (R^2 = 0.9944) and more accurately captured the entire kinetic profile. The very high initial adsorption rate parameter (α = 624.432 mg g^{-1} min^{-1}) indicates rapid initial uptake, while the desorption constant β = 0.110 g mg^{-1} suggests a moderate surface coverage effect. The excellent agreement with the Elovich model supports the presence of a heterogeneous surface with variable energy sites, consistent with EZ$_{TPA}$50's amorphous structure and mesoporosity.

Table 5 Pseudo-first order, pseudo-second order, Elovich and intraparticle diffusion kinetic model parameters for MB adsorption onto EZTPA100 and EZTPA50

Kinetic model		EZ$_{TPA}$100	EZ$_{TPA}$50
Pseudo-first order			
k_1	min^{-1}	0.05717	0.20057
$q_e/q_{e\,(exp)}$	mg g^{-1}	67.97/77.12	80.27/89.23
R^2		0.9011	0.7846
Pseudo-second order			
k_2	g (mg min)$^{-1}$	0.00691	0.00357
$q_e/q_{e\,(exp)}$	mg g^{-1}	77.43/77.12	84.54/89.23
R^2		0.9504	0.9053
Elovich			
α	mg g^{-1} min^{-1}	17.784	624.432
β	g mg^{-1}	0.079	0.110
R^2		0.9938	0.9944
Intraparticle diffusion			
Stage 1			
k_{id}	mg g^{-1} min$^{-1/2}$	7.747	6.497
C	mg g^{-1}	7.919	32.014
R^2		0.9969	0.9811
Stage 2			
k_{id}	mg g^{-1} min$^{-1/2}$	2.509	1.741
C	mg g^{-1}	36.021	63.076
R^2		0.9962	0.9827
Stage 3			
k_{id}	mg g^{-1} min$^{-1/2}$	0.780	0.162
C	mg g^{-1}	63.5886	86.336
R^2		0.9995	0.9496

For EZ$_{TPA}$100, the PFO model produced a better fit than for EZ$_{TPA}$50 (R^2 = 0.9011), yet still underestimated the experimental adsorption capacity (q_e = 67.97 *vs.* $q_{e,exp}$ = 77.12 mg g^{-1}). The PSO model further improved the correlation (R^2 = 0.9504) and yielded a calculated q_e value (77.43 mg g^{-1}) in excellent agreement with the experimental result, suggesting a stronger chemisorption contribution in EZ$_{TPA}$100 than in EZ$_{TPA}$50. Nevertheless, the Elovich model again provided the best overall fit (R^2 = 0.9938) with kinetic constants (α = 17.784 mg g^{-1} min^{-1} and β = 0.079 g mg^{-1}), indicating a lower initial chemisorption rate and a more uniform adsorption surface compared to EZ$_{TPA}$50.

The intraparticle diffusion (IPD) model was employed to gain deeper insight into the adsorption kinetics of methylene blue (MB) onto EZ$_{TPA}$50 and EZ$_{TPA}$100. The resulting plots for q_t

versus $t^{1/2}$ revealed a characteristic three-stage behavior for both materials, indicative of a multi-mechanistic adsorption process involving surface adsorption, pore diffusion, and eventual equilibrium (Fig. 9).

In stage 1, attributed to external surface adsorption, $EZ_{TPA}100$ exhibited a higher diffusion rate constant ($k_{id,1}$ = 7.747 mg g^{-1} $min^{-1/2}$) compared to $EZ_{TPA}50$ ($k_{id,1}$ = 6.497 mg g^{-1} $min^{-1/2}$), reflecting a steeper initial kinetic slope. However, despite this higher rate constant, $EZ_{TPA}50$ adsorbed significantly more dye at the earliest measured time point (2 minutes), reaching approximately 40 mg g^{-1} – substantially higher than $EZ_{TPA}100$ at the same time. This apparent discrepancy is not contradictory but reflects the influence of the intercept C, which was notably larger for $EZ_{TPA}50$ (32.014 mg g^{-1}) than for $EZ_{TPA}100$ (7.919 mg g^{-1}). While k_{id} quantifies the rate of intraparticle transport, the intercept captures the initial mass accumulation in the boundary layer and on the external surface. The high C value for $EZ_{TPA}50$ suggests a rapid initial uptake due to a higher density of readily accessible active sites or stronger dye–adsorbent interactions. Furthermore, stage 1 was longer in duration for $EZ_{TPA}50$ than for $EZ_{TPA}100$, suggesting that surface adsorption dominated for a more extended period, possibly due to a greater availability of active surface sites or slower saturation dynamics. In contrast, $EZ_{TPA}100$ transitioned more rapidly into the pore diffusion phase, which may indicate faster initial surface site saturation or more limited external adsorption capacity. Both materials showed excellent linearity (R^2 = 0.9969 for $EZ_{TPA}100$; R^2 = 0.9811 for $EZ_{TPA}50$), confirming efficient film diffusion in this stage.

In stage 2, associated with gradual intraparticle diffusion into meso- and microporous domains, $EZ_{TPA}100$ again showed a higher diffusion rate constant ($k_{id,2}$ = 2.509 *vs.* 1.741 mg g^{-1} $min^{-1/2}$) and the diffusion phase extended over a longer time interval. In contrast, $EZ_{TPA}50$ progressed through stage 2 more rapidly, despite exhibiting a larger intercept (C = 63.076 mg g^{-1} *vs.* 36.021 mg g^{-1}), suggesting that its internal structure may allow more efficient pore access or faster dye equilibration despite the slower diffusion rate. In stage 3, representing the equilibrium region, $EZ_{TPA}100$ maintained a higher diffusion constant ($k_{id,3}$ = 0.780 *vs.* 0.162 mg g^{-1} $min^{-1/2}$), while $EZ_{TPA}50$ exhibited the highest intercept of all stages (C = 86.336 mg g^{-1} *vs.* 63.589 mg g^{-1}), consistent with a more prolonged approach to saturation and continued dye retention on high-affinity sites.

Overall, the superior fit of the Elovich model for both materials suggests that the adsorption of methylene blue proceeds *via* a complex, surface-mediated mechanism governed by heterogeneous site energies and diffusion-limited uptake. While traditionally associated with chemisorption, the Elovich behavior observed here likely reflects the structural disorder and energetic variability of the embryonic zeolites, rather than true chemical bonding. While $EZ_{TPA}100$ exhibits more consistent diffusion behavior and a slightly better fit to PSO kinetics, $EZ_{TPA}50$ demonstrates faster initial uptake and higher overall adsorption capacity, reflecting a greater density of active sites and more heterogeneous surface chemistry. These findings are consistent with the structural data—such as higher BET surface area, broader pore size distribution, and greater particle size heterogeneity—observed for $EZ_{TPA}50$, which collectively promote rapid dye binding and enhanced adsorption performance. The intraparticle diffusion (IPD) model further supports this interpretation by revealing a multi-stage adsorption process, where $EZ_{TPA}50$ displays a shorter diffusion pathway and larger boundary layer contribution, leading to faster saturation of active sites despite a lower diffusion rate constant. This makes $EZ_{TPA}50$ particularly advantageous under conditions requiring rapid dye removal within limited contact times.

Thermodynamic studies

Thermodynamic studies were performed at different temperatures (25, 35 and 45 °C), and the resulting equilibrium data were used to calculate key thermodynamic parameters using the Van't Hoff approach. This method enables the calculation of the Gibbs free energy change (ΔG°), enthalpy change (ΔH°), and entropy change (ΔS°), which together provide insight into the spontaneity, energy changes, and interfacial disorder associated with the adsorption process. These thermodynamic quantities were calculated using the Van't Hoff equation (eqn (11)) and the standard Gibbs free energy relation (eqn (12)), based on the temperature dependence of the equilibrium constant:

$$\ln K_c = -\frac{\Delta H^\circ}{R}\frac{1}{T} + \frac{\Delta S^\circ}{R} \tag{11}$$

$$\Delta G^\circ = -RT\ln K_c \tag{12}$$

where K_c is equilibrium constant ($K_c = q_e/C_e$), ΔH° is the enthalpy change (kJ mol^{-1}), ΔS° is the entropy change (J mol^{-1} K^{-1}), ΔG° is the Gibbs free energy change, R is the universal gas constant (8.314 J mol^{-1} K^{-1}), and T is the absolute temperature (K).

The Van't Hoff plots ($\ln K$ *vs.* $1/T$) yielded linear fits with high correlation coefficients, particularly for $EZ_{TPA}100$ (R^2 = 0.9982), indicating a reliable thermodynamic model (Fig. S9). The calculated values for ΔG°, ΔH°, and ΔS° for $EZ_{TPA}50$ and $EZ_{TPA}100$ are summarized in Table 6. For $EZ_{TPA}50$, the adsorption process was found to be endothermic, with a positive enthalpy (ΔH = 42.92 kJ mol^{-1}) and entropy change (ΔS° = 167.63 J mol^{-1} K^{-1}), suggesting increased randomness at the solid–liquid interface. The negative values of ΔG° at all tested temperatures (−7.04 to −10.39 kJ mol^{-1}) confirm that the adsorption is spontaneous and becomes more favorable with increasing temperature. Similarly, $EZ_{TPA}100$ exhibited an even higher endothermicity (ΔH° = 79.93 kJ mol^{-1}) and greater entropy gain (ΔS° = 283.0 J mol^{-1} K^{-1}), consistent with enhanced dye–adsorbent interactions and significant structural reorganization at the interface.

The corresponding ΔG° values (−4.40 to −10.06 kJ mol^{-1}) further reinforce the spontaneity and temperature-dependent favorability of the process. Although the ΔH° for $EZ_{TPA}100$ approaches the lower threshold typically associated with chemisorption, the overall values for both samples remain closer to those characteristic of physisorption (<40–80 kJ mol^{-1}).

This suggests that adsorption is predominantly physisorptive and entropy-driven, with a possible minor contribution

Table 6 Thermodynamic parameters for the adsorption of methylene blue onto $EZ_{TPA}50$ and $EZ_{TPA}100$, calculated from van't Hoff plots

			ΔG°, kJ mol^{-1}			
	ΔH° kJ mol^{-1}	ΔS° J mol^{-1} K^{-1}	298 K	308 K	318 K	R^2
$EZ_{TPA}100$	79.93	283.0	−4.40	−7.23	−10.06	0.998
$EZ_{TPA}50$	42.92	167.63	−7.04	−8.72	−10.39	0.944

from weak chemisorption in the case of $EZ_{TPA}100$. However, this interpretation is indirect and should be validated by spectroscopic analysis (*e.g.*, XPS or FTIR before and after adsorption) in future work. Taken together, the thermodynamic and kinetic data highlight the role of surface heterogeneity and thermal activation in modulating dye uptake on disordered zeolite frameworks, but confirm that physisorption remains the dominant adsorption pathway

Regeneration studies

The thermodynamic and kinetic results suggest that adsorption is predominantly physisorptive, with possible minor contributions from weak chemisorption in the case of $EZ_{TPA}100$. These mechanistic insights imply that desorption *via* conventional regeneration methods such as solvent rinsing or acid/base treatment may be insufficient due to surface-level retention and diffusion limitations. Therefore, given the high thermal stability of the EZPs, which retain structural integrity up to at least 600 °C, thermal regeneration was selected as a robust and effective strategy. Spent adsorbents were thermally treated in static air at 550 °C for 4 h, resulting in complete oxidative decomposition of methylene blue (Fig. 10a).

Regeneration performance was assessed over four consecutive adsorption–desorption cycles under the optimized adsorption conditions (C_0 = 50 mg L^{-1}, pH = 7, 0.01 M NaCl, stirring speed = 250 rpm, temperature = 25 °C, and contact time = 4 h). As illustrated in Fig. 10b, $EZ_{TPA}50$ maintained high removal efficiency (∼90%) across all cycles, confirming its excellent thermal resilience and surface stability. In contrast, $EZ_{TPA}100$ exhibited a gradual decline in performance, dropping from ∼77% in the first cycle to ∼55% by the fourth. This reduction may be attributed to partial structural reorganization or pore collapse during repeated calcination, which likely affects the accessibility and integrity of active sites. The relatively weaker framework stability of $EZ_{TPA}100$ compared to $EZ_{TPA}50$ suggests that differences in textural robustness play a critical role in determining long-term reusability of embryonic zeolites under high-temperature regeneration protocols.

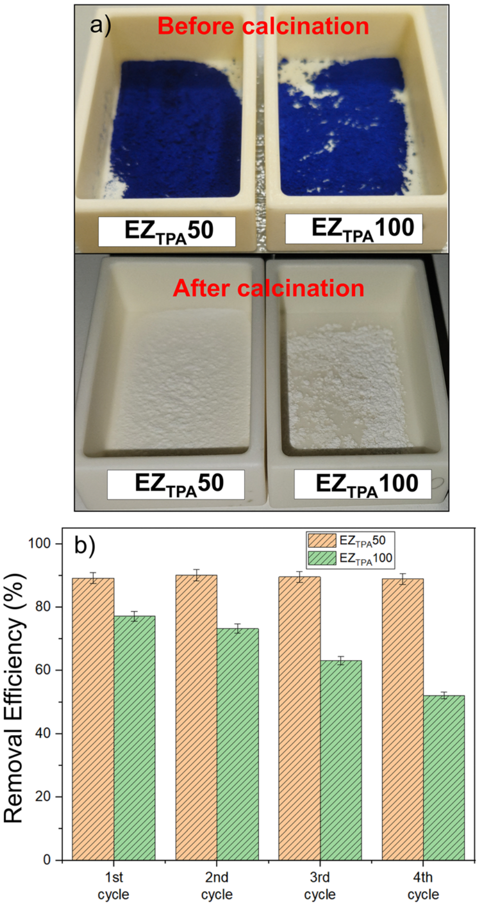

Fig. 10 Adsorbents' appearance before and after the first regeneration cycle performed at 550 °C for 4 h (a) and (b) removal efficiencies of $EZ_{TPA}50$ and $EZ_{TPA}100$ after four regeneration cycles at optimal conditions.

Table 7 provides a comparative overview of methylene blue adsorption capacities, experimental conditions, kinetic models, and regeneration performance reported for various adsorbents. Embryonic zeolite precursors distinguish themselves by combining high adsorption capacities with excellent thermal regeneration stability, retaining up to 90% efficiency over multiple cycles. Unlike many conventional or composite materials that either suffer from poor reusability or demand complex regeneration protocols, EZPs offer strong dye uptake together with structural robustness and ease of recovery, making them attractive for sustainable water treatment.

In addition to adsorption and regeneration performance, scalability and economic aspects are critical for practical deployment. While tetrapropylammonium hydroxide (TPAOH) is more expensive than the precursors commonly used for activated carbons or commercial zeolites, it was employed here in moderate quantities and could be recycled or replaced in future process optimizations. Compared with advanced frameworks such as MOFs and COFs, EZPs require far simpler processing yet deliver competitive performance and excellent reusability. These attributes indicate that EZPs strike a favorable balance between efficiency, stability, and cost, reinforcing their potential as viable candidates for real-world water treatment applications.

Experimental

Materials and methods

All reagents used for synthesis and adsorption experiments were purchased from Merck and ThermoFisher scientific and were used without further purification.

Table 7 Comparison of the Langmuir maximum adsorption capacity, experimental and regeneration conditions of various adsorbents for MB removal

Adsorbent	q_{max} mg g^{-1}	Experimental conditions		Kinetic model	Regeneration		Ref.
EZ$_{TPA}$50	146.08	Dose: 0.5 g L^{-1} C_0: 50 mg L^{-1}	240 min, pH 7 T: 25 °C	Elovich	550 °C 4 h	Const. 90% 4 cycles	This study
EZ$_{TPA}$100	122.62					77% → 55% 4 cycles	
Mn/MCM-41	45.38	Dose: 1 g L^{-1} C_0 : 50 mg L^{-1}	120 min, pH 6.3 T: 25 °C	PSO	—		35
3.3% Fe_3O_4/NaA	40.36	Dose: 7.2 g L^{-1} C_0: 300 mg L^{-1}	120 min, pH 8.6 T: 25 °C	PSO	—		53
Ni/Co USY	59.80	Dose: 2 g L^{-1} C_0: 100 mg L^{-1}	120 min, pH 8 T: 25 °C	PSO	700 °C 6 h	> 90%, 2 cycles	37
Nanosheet MFI	227.70	Dose: 0.5 g L^{-1} C_0: 25 mg L^{-1}	10 min, pH 10 T: 25 °C	PSO	Acid wash	99% → 85% 5 cycles	54
NZVI/SuZSM	86.96	Dose: 5 g L^{-1} C_0: 20 mg L^{-1}	90 min, pH 7 T: 25 °C	PSO		96% → 23% 3 cycles	36
Coir pith carbon	5.87	Dose: 2 g L^{-1} C_0: 10–40 mg L^{-1}	40 min, pH 6.9 T: 25 °C	PSO	—		33
Graphene	153.85	Dose: 0.1 g L^{-1} C_0: 20–40 mg L^{-1}	1500 min, pH 10 T: 25 °C	—	—		34
Algerian kaolinite	64.58	Dose: 1 g L^{-1} C_0: 50–200 mg L^{-1}	200 min, pH 4 T: 25 °C	PSO	—		38
Green Peel material	207.90	Dose: 0.6 g L^{-1} C_0: 400 mg L^{-1}	30 min, pH 6.6 T: 25 °C	PSO	EtOH wash	79% → 15% 5 cycles	55
(C-Si@GS)	456.8	Dose: 0.6 g L^{-1} C_0: 120 mg L^{-1}	720 min, pH 7 T: 25 °C	PSO	HCl wash	99% → 50% 3 cycles	56

Powder X-ray diffraction (PXRD) and small-angle X-ray scattering (SAXS) analyses were performed using an Empyrean diffractometer (Malvern Panalytical, Netherlands) equipped with a Cu Kα radiation source (λ = 1.5418 Å) and a PIXcel3D detector. PXRD patterns of the embryonic zeolite precursors were recorded over the 2θ range of 2°–50°, while SAXS measurements were conducted in the low-angle range of 0°–5° 2θ with a step size of 0.01°. The instrument was operated at 45 kV and 40 mA. SAXS data were analyzed using EasySAXS ver 2.2 software (Malvern Panalytical, Netherlands). Elemental composition was determined using an Epsilon-1 energy-dispersive X-ray fluorescence (EDXRF) spectrometer (Malvern Panalytical, Netherlands) equipped with Omnian software for standardless quantification. Samples were finely ground and placed in a holder in the form of loose powder. Measurements were performed under ambient conditions using a silver (Ag) anode X-ray tube. The instrument's software automatically optimized the operating voltage and current based on the elements of interest. Surface area and porosity of the adsorbents were characterized by nitrogen (N_2) adsorption–desorption measurements at 77 K using a 3Flex surface analyzer (Micromeritics, Norcross, GA, USA) and Flex v6.02 as data acquisition and processing software. Prior to analysis, samples were degassed under vacuum ($> 1.10^{-5}$ mmHg) at 300 °C for 4 h to remove adsorbed gases and moisture. The specific surface area was calculated using the Brunauer–Emmett–Teller[57] method in the relative pressure (P/P_0) range of 0.05–0.30 or 0.01–0.12 (for microporous materials following the Rouquerol criteria).[58] Micropore volume and external surface area were estimated by t-plot analysis using the Harkins and Jura thickness equation.[59,60] Pore size distribution was determined by density functional theory (DFT) analysis of the N_2 adsorption–desorption branch of the isotherms, using the cylindrical oxide pore model with strong potential (N_2@77 K DFT) and a regularization parameter of 0.01.[61] Total pore volume was estimated from the amount of N_2 adsorbed at $P/P_0 \approx 0.96$. The infrared spectra were collected on Tensor 37 (Bruker, Berlin, Germany) spectrometer using KBr pellets. For each sample, 128 scans were collected at a resolution of 2 cm^{-1} over the wavenumber region 4000–400 cm^{-1}. Simultaneous thermogravimetric and differential scanning calorimetry analyses (TGA/DSC) were performed using a BXT-STA-200 analyzer (Shanghai Glomro). Twenty mg of each sample was weighed in corundum crucibles and examined in the temperature range of 25–600 °C, heating rate of 10 °C min^{-1}, and with a dynamic air atmosphere. The NMR spectra were recorded on a Bruker Avance III HD 500 NMR spectrometer (Bruker, Karlsruhe, Germany) operating at 500.13 MHz ^{1}H frequency (99.35 MHz for ^{29}Si, 130.31 for ^{27}Al), using a 2.5 mm solid- state CP/MAS dual ^{1}H/^{31}P–^{15}N probe head. The samples were packed in 2.5 mm rotors (ZrO_2) and spun at a magic angle spinning (MAS) rate of 20 kHz for both ^{29}Si and ^{27}Al experiments. The quantitative direct excitation ^{29}Si NMR spectra were acquired with a single-pulse sequence, 90° pulse length of 1.75 μs, time domain data points of 4 K, spectrum width of 37 kHz, and 384 transients were accumulated with a relaxation delay of 30 s between each scan. ^{27}Al spectra were acquired with a single pulse sequence, 90° pulse length of 2.4 μs, 4 K time domain data points, spectrum width of 250 kHz, 1024 scans, and a relaxation delay of 0.5 s. The NMR spectra were deconvoluted in Origin (OriginLab, Northampton, MA, USA) using Voigt line-shape functions, which allowed reliable separation of overlapping resonances. The structural features of embryonic zeolites were studied by HRTEM. The analyses were performed at room temperature in low-dose mode at 300 kV accelerating voltage in a FEI-Philips CM300 TEM, equipped with a LaB_6 cathode. Suspension in distilled water was prepared from the solid powder samples without any grinding. After ultrasonication to break up large aggregates a droplet of the suspension was deposited onto holey-carbon coated Cu grids. UV/Vis spectroscopic analyses were performed on a Cary 4000 spectrophotometer (Agilent, Santa Clara, CA, USA). The absorbance of methylene blue (MB) solutions was measured at $\lambda_{\max} = 664$ nm to determine residual dye concentrations. Calibration curves were constructed using standard MB solutions in the concentration range of 1–10 mg L^{-1}, yielding linear relationships with correlation coefficients exceeding 0.999. Prior to each measurement, the samples were centrifuged at 14 000 rpm for 1 min to remove suspended adsorbent particles, and the supernatants were analyzed without further dilution unless absorbance exceeded the linear range of the instrument. All measurements were performed in triplicate, and average absorbance values were used to calculate adsorption capacities and removal efficiencies.

Conclusions

This study systematically investigated the adsorption behavior of embryonic zeolite precursors toward methylene blue (MB) under aqueous conditions, with particular emphasis on structure–function relationships, adsorption mechanisms, and regeneration performance. The results demonstrated that tailoring the Si/Al ratio during the synthesis significantly affects the physicochemical properties of the materials, including surface area, pore structure, particle size distribution, and surface charge. Among the tested samples, $EZ_{TPA}50$ exhibited the most favorable characteristics—namely, a hierarchically porous structure, high BET surface area, and low point of zero charge—leading to superior adsorption capacity (146.08 mg g^{-1}) and faster dye uptake compared to $EZ_{TPA}100$ (122.62 mg g^{-1}) and crystalline H-ZSM-5 (80.53 mg g^{-1}) used as reference.

Adsorption isotherm modeling revealed that the Langmuir model best described the equilibrium data, indicating monolayer adsorption behavior, while surface coverage analysis highlighted the importance of pore accessibility in determining adsorption efficiency. Kinetic studies showed excellent agreement with the Elovich model, consistent with adsorption on energetically heterogeneous surfaces. Thermodynamic analysis confirmed that the adsorption process is spontaneous, endothermic, and entropy-driven for both $EZ_{TPA}50$ and $EZ_{TPA}100$, suggesting a predominantly physisorptive process with a possible minor contribution from weak chemisorption in the case of $EZ_{TPA}100$. Taken together, these results point to physisorption as the dominant mechanism, modulated by surface heterogeneity and thermal activation effects, although further spectroscopic studies will be needed to confirm the exact nature of dye–surface interactions. Thermal regeneration studies revealed that $EZ_{TPA}50$ retained removal efficiencies ∼90% across four adsorption–desorption cycles, while $EZ_{TPA}100$ showed a gradual decline, likely due to partial structural collapse during calcination. This difference underscores the role of textural robustness in determining long-term reusability. Overall, the findings highlight embryonic zeolites – particularly $EZ_{TPA}50$ – as a promising, regenerable, and high-capacity adsorbent for the removal of organic dyes from contaminated water, offering a compelling alternative to conventional microporous zeolites. This work represents the first systematic application of embryonic zeolites in dye remediation and provides a foundation for the development of next-generation adsorbents for water treatment applications. Future perspectives include validating the performance of EZPs in real wastewater matrices containing mixed dyes, natural organic matter, and competing inorganic ions. Such studies will enable a realistic assessment of their adsorption efficiency and selectivity under complex conditions, strengthening their prospects for industrial wastewater treatment and environmental remediation.

Author contributions

Conceptualization R. R. and V. V.; formal analysis R. R. and H. L.; investigation R. R., H. L., M. A., N. P.; methodology R. R., H. L., M. A., visualization R. R., H. L. and M. A. writing – original draft – R. R., H. L., M. A.; writing – review & editing V. V. and R. N.; supervision V. V.; resources V. V. and R. N.; project administration – V. V. and R. N. All authors have read and agreed to the published version of the manuscript.

Conflicts of interest

There are no conflicts to declare.

Data availability

The data supporting this article have been included as part of the supplementary information (SI). Supplementary information is available. See DOI: **https://doi.org/10.1039/d5ma00944h**.

Acknowledgements

The authors acknowledge the financial support from the European Union-NextGenerationEU through the National Recovery and Resilience Plan of the Republic of Bulgaria, project No. BG-RRP-2.004-0008.

References

1 N. Tüfekci, N. Sivri and İ. Toroz, Pollutants of textile industry wastewater and assessment of its discharge limits by water quality standards, *Turk. J. Fish. Aquat. Sci.*, 2007, **7**, 97–103.

2 F. Uddin, Environmental hazard in textile dyeing wastewater from local textile industry, *Cellulose*, 2021, **28**, 10715–10739.

3 S. Mehra, M. Singh and P. Chadha, Adverse impact of textile dyes on the aquatic environment as well as on human beings, *Toxicol. Int.*, 2021, **28**, 165.

4 T. Akter, A. T. Protity, M. Shaha, M. Al Mamun and A. Hashem, *Nanohybrid materials for treatment of textiles dyes*, Springer, 2023, pp. 401–431.

5 C. Y. Teh, P. M. Budiman, K. P. Y. Shak and T. Y. Wu, Recent advancement of coagulation–flocculation and its

application in wastewater treatment, *Ind. Eng. Chem. Res.*, 2016, **55**, 4363–4389.

6 S. Varjani, P. Rakholiya, H. Y. Ng, S. You and J. A. Teixeira, Microbial degradation of dyes: An overview, *Bioresour. Technol.*, 2020, **314**, 123728.

7 G. M. Didier de Vasconcelos, J. Mulinari, S. M. de Arruda Guelli Ulson de Souza, A. A. Ulson de Souza, D. de Oliveira and C. J. de Andrade, Biodegradation of azo dye-containing wastewater by activated sludge: a critical review, *World J. Microbiol. Biotechnol.*, 2021, **37**, 101.

8 S. Khan, T. Noor, N. Iqbal and L. Yaqoob, Photocatalytic dye degradation from textile wastewater: a review, *ACS Omega*, 2024, **9**, 21751–21767.

9 K. O. Iwuozor, Prospects and challenges of using coagulation-flocculation method in the treatment of effluents, *Adv. J. Chem., Sect. A*, 2019, **2**, 105–127.

10 K. H. D. Tang, N. M. Darwish, A. M. Alkahtani, M. R. AbdelGawwad and P. Karácsony, Biological removal of dyes from wastewater: a review of its efficiency and advances, *Trop. Aquat. Soil Pollut.*, 2022, **2**, 59–75.

11 H. Hauduc, L. Rieger, A. Oehmen, M. Van Loosdrecht, Y. Comeau, A. Héduit, P. Vanrolleghem and S. Gillot, Critical review of activated sludge modeling: state of process knowledge, modeling concepts, and limitations, *Biotechnol. Bioeng.*, 2013, **110**, 24–46.

12 B. Viswanathan, Photocatalytic degradation of dyes: an overview, *Curr. Catal.*, 2018, **7**, 99–121.

13 Z. A. Hammood, T. F. Chyad and R. Al-Saedi, Adsorption performance of dyes over zeolite for textile wastewater treatment, *Ecol. Chem. Eng.*, 2021, **28**, 329–337.

14 J. Weitkamp, Zeolites and catalysis, *Solid State Ionics*, 2000, **131**, 175–188.

15 C. J. Rhodes, Properties and applications of zeolites, *Sci. Prog.*, 2010, **93**, 223–284.

16 V. Gadore, S. R. Mishra, N. Yadav, G. Yadav and M. Ahmaruzzaman, Advances in zeolite-based materials for dye removal: Current trends and future prospects, *Inorg. Chem. Commun.*, 2024, **166**, 112606.

17 T. Bajda, A. Grela, J. Pamuła, J. Kuc, A. Klimek, J. Matusik, W. Franus, S. K. K. Alagarsamy, T. Danek and P. Gara, Using zeolite materials to remove pharmaceuticals from water, *Materials*, 2024, **17**, 3848.

18 Y. Li, L. Li and J. Yu, Applications of zeolites in sustainable chemistry, *Chem*, 2017, **3**, 928–949.

19 E. Pérez-Botella, S. Valencia and F. Rey, Zeolites in adsorption processes: State of the art and future prospects, *Chem. Rev.*, 2022, **122**, 17647–17695.

20 B. Yue, S. Liu, Y. Chai, G. Wu, N. Guan and L. Li, Zeolites for separation: Fundamental and application, *J. Energy Chem.*, 2022, **71**, 288–303.

21 L. F. de Magalhães, G. R. da Silva and A. E. C. Peres, Zeolite application in wastewater treatment, *Adsorpt. Sci. Technol.*, 2022, **2022**, 4544104.

22 R. Bingre, B. Louis and P. Nguyen, An overview on zeolite shaping technology and solutions to overcome diffusion limitations, *Catalysts*, 2018, **8**, 163.

23 X. Tan, Y. Liu, G. Zeng, X. Wang, X. Hu, Y. Gu and Z. Yang, Application of biochar for the removal of pollutants from aqueous solutions, *Chemosphere*, 2015, **125**, 70–85.

24 M. Ahmad, A. U. Rajapaksha, J. E. Lim, M. Zhang, N. Bolan, D. Mohan, M. Vithanage, S. S. Lee and Y. S. Ok, Biochar as a sorbent for contaminant management in soil and water: a review, *Chemosphere*, 2014, **99**, 19–33.

25 J.-R. Li, R. J. Kuppler and H.-C. Zhou, Selective gas adsorption and separation in metal–organic frameworks, *Chem. Soc. Rev.*, 2009, **38**, 1477–1504.

26 J. Abdi, M. Vossoughi, N. M. Mahmoodi and I. Alemzadeh, Synthesis of metal-organic framework hybrid nanocomposites based on GO and CNT with high adsorption capacity for dye removal, *Chem. Eng. J.*, 2017, **326**, 1145–1158.

27 S.-Y. Ding and W. Wang, Covalent organic frameworks (COFs): from design to applications, *Chem. Soc. Rev.*, 2013, **42**, 548–568.

28 X. Zhu, S. An, Y. Liu, J. Hu, H. Liu, C. Tian, S. Dai, X. Yang, H. Wang and C. W. Abney, Efficient removal of organic dye pollutants using covalent organic frameworks, *AIChE J.*, 2017, **63**, 3470–3478.

29 M. Akouche, J.-P. Gilson, N. Nesterenko, S. Moldovan, D. Chateigner, H. E. Siblani, D. Minoux, J.-P. Dath and V. Valtchev, Synthesis of embryonic zeolites with controlled physicochemical properties, *Chem. Mater.*, 2020, **32**, 2123–2132.

30 A. Palčić, S. N. Jaén, D. Wu, M. Cai, C. Liu, E. A. Pidko, A. Y. Khodakov, V. Ordomsky and V. Valtchev, Embryonic zeolites for highly efficient synthesis of dimethyl ether from syngas, *Microporous Mesoporous Mater.*, 2021, **322**, 111138.

31 K.-G. Haw, J.-P. Gilson, N. Nesterenko, M. Akouche, H. El Siblani, J.-M. Goupil, B. Rigaud, D. Minoux, J.-P. Dath and V. Valtchev, Supported embryonic zeolites and their use to process bulky molecules, *ACS Catal.*, 2018, **8**, 8199–8212.

32 K.-G. Haw, J.-M. Goupil, J.-P. Gilson, N. Nesterenko, D. Minoux, J.-P. Dath and V. Valtchev, Embryonic ZSM-5 zeolites: zeolitic materials with superior catalytic activity in 1, 3, 5-triisopropylbenzene dealkylation, *New J. Chem.*, 2016, **40**, 4307–4313.

33 D. Kavitha and C. Namasivayam, Experimental and kinetic studies on methylene blue adsorption by coir pith carbon, *Bioresour. Technol.*, 2007, **98**, 14–21.

34 Y. Yasin, M. Z. Hussein and F. H. Ahmad, Adsorption of methylene blue onto treated activated carbon, *Malays. J. Anal. Sci.*, 2007, **11**, 400–406.

35 Y. Shao, X. Wang, Y. Kang, Y. Shu, Q. Sun and L. Li, Application of Mn/MCM-41 as an adsorbent to remove methyl blue from aqueous solution, *J. Colloid Interface Sci.*, 2014, **429**, 25–33.

36 A. K. Hammed, N. Dewayanto, D. Du, M. H. Ab Rahim and M. R. Nordin, Novel modified ZSM-5 as an efficient adsorbent for methylene blue removal, *J. Environ. Chem. Eng.*, 2016, **4**, 2607–2616.

37 S. Oukil, F. Bali and D. Halliche, Adsorption and kinetic studies of methylene blue on modified HUSY zeolite and an amorphous mixture of γ-alumina and silica, *Sep. Sci. Technol.*, 2020, **55**, 2642–2658.

38 N. Hamri, A. Imessaoudene, A. Hadadi, S. Cheikh, A. Boukerroui, J.-C. Bollinger, A. Amrane, H. Tahraoui, H. N. Tran and A. O. Ezzat, Enhanced adsorption capacity of methylene blue dye onto kaolin through acid treatment: batch adsorption and machine learning studies, *Water*, 2024, **16**, 243.

39 T. Armaroli, L. Simon, M. Digne, T. Montanari, M. Bevilacqua, V. Valtchev, J. Patarin and G. Busca, Effects of crystal size and Si/Al ratio on the surface properties of H-ZSM-5 zeolites, *Appl. Catal., A*, 2006, **306**, 78–84.

40 Y. Gao, B. Zheng, G. Wu, F. Ma and C. Liu, Effect of the Si/Al ratio on the performance of hierarchical ZSM-5 zeolites for methanol aromatization, *RSC Adv.*, 2016, **6**, 83581–83588.

41 P. Hudec, A. Smiešková, Z. Židek, M. Zúbek, P. Schneider, M. Kočiřík and J. Kozánková, Adsorption properties of ZSM-5 zeolites, *Collect. Czech. Chem. Commun.*, 1998, **63**, 141–154.

42 W. Song, R. Justice, C. Jones, V. Grassian and S. Larsen, Synthesis, characterization, and adsorption properties of nanocrystalline ZSM-5, *Langmuir*, 2004, **20**, 8301–8306.

43 Z. Cheng, H. Shan, Y. Sun, L. Zhang, H. Jiang and C. Li, Evolution mechanism of surface hydroxyl groups of silica during heat treatment, *Appl. Surf. Sci.*, 2020, **513**, 145766.

44 M. K. Król and P. Jeleń, The effect of heat treatment on the structure of zeolite A, *Materials*, 2021, **14**, 4642.

45 N. Fiol and I. Villaescusa, Determination of sorbent point zero charge: usefulness in sorption studies, *Environ. Chem. Lett.*, 2009, **7**, 79–84.

46 S. M. Turp, G. A. Turp, N. Ekinci and S. Özdemir, Enhanced adsorption of methylene blue from textile wastewater by using natural and artificial zeolite, *Water Sci. Technol.*, 2020, **82**, 513–523.

47 L. Zhang, W. Huang, X. Dong, Y. Zhao, F.-F. Li and Q.-H. Cen, Improvement of zeolite adsorption ability for methylene blue by using electrospinning cellulose microfibers as template, *Water, Air, Soil Pollut.*, 2024, **235**, 102.

48 T. A. Osmari, R. Gallon, M. Schwaab, E. Barbosa-Coutinho, J. B. Severo Jr and J. C. Pinto, Statistical analysis of linear and non-linear regression for the estimation of adsorption isotherm parameters, *Adsorpt. Sci. Technol.*, 2013, **31**, 433–458.

49 R. Vitek and J. C. Masini, Nonlinear regression for treating adsorption isotherm data to characterize new sorbents: Advantages over linearization demonstrated with simulated and experimental data, *Heliyon*, 2023, **9**, e15128.

50 E. D. Revellame, D. L. Fortela, W. Sharp, R. Hernandez and M. E. Zappi, Adsorption kinetic modeling using pseudo-first order and pseudo-second order rate laws: A review, *Cleaner Eng. Technol.*, 2020, **1**, 100032.

51 C. Aharoni and F. Tompkins, *Advances in catalysis*, Elsevier, 1970, vol. 21, pp. 1–49.

52 F.-C. Wu, R.-L. Tseng and R.-S. Juang, Initial behavior of intraparticle diffusion model used in the description of adsorption kinetics, *Chem. Eng. J.*, 2009, **153**, 1–8.

53 N. B. T. Tran, N. B. Duong and N. L. Le, Synthesis and characterization of magnetic Fe3O4/zeolite NaA nanocomposite for the adsorption removal of methylene blue potential in wastewater treatment, *J. Chem.*, 2021, **2021**, 6678588.

54 Y. Ji, F. Xu, W. Wei, H. Gao, K. Zhang, G. Zhang, Y. Xu and P. Zhang, Efficient and fast adsorption of methylene blue dye onto a nanosheet MFI zeolite, *J. Solid State Chem.*, 2021, **295**, 121917.

55 O. R. Benkouachi, A. Bouguettoucha, H. Tahraoui, A. Guediri, D. Chebli, M. Kebir, S. Knani, J. Zhang and A. Amrane, Advanced green peel utilization for efficient methylene blue removal: integrated analysis and predictive modeling, *J. Mol. Liq.*, 2024, **413**, 125951.

56 Z. Li, Y. Chen, D. Wang, K. Yang and J. Sun, Synthesis of composites from coal gasification slag by acid leaching and NaOH activation for efficient adsorption of methylene blue, *Appl. Surf. Sci.*, 2025, **679**, 161186.

57 D. Dollimore, P. Spooner and A. Turner, The bet method of analysis of gas adsorption data and its relevance to the calculation of surface areas, *Surf. Technol.*, 1976, **4**, 121–160.

58 J. Rouquerol, P. Llewellyn and F. Rouquerol, *Studies in surface science and catalysis*, Elsevier, 2007, vol. 160, pp. 49–56.

59 P. Hudec, A. Smiešková, P. Schneider and O. Ŝolcová, *Studies in surface science and catalysis*, Elsevier, 2002, vol. 142, pp. 1587–1594.

60 W. D. Harkins and G. Jura, Surface of solids. X. Extension of the attractive energy of a solid into an adjacent liquid or film, the decrease of energy with distance, and the thickness of films, *J. Am. Chem. Soc.*, 1944, **66**, 919–927.

61 P. I. Ravikovitch, G. L. Haller and A. V. Neimark, Density functional theory model for calculating pore size distributions: pore structure of nanoporous catalysts, *Adv. Colloid Interface Sci.*, 1998, **76**, 203–226.